Dislocation–grain boundary interaction-based discrete dislocation dynamics modeling and its application to bicrystals with different misorientations

Xu Zhang [a], Songjiang Lu [a], Bo Zhang [a], Xiaobao Tian [b], Qianhua Kan [a], Guozheng Kang [a*],

[a] *Applied Mechanics and Structure Safety Key Laboratory of Sichuan Province, School of Mechanics and Engineering, Southwest Jiaotong University, Chengdu, 610031, China*

[b] *Department of Mechanics, Sichuan University, Chengdu, 610065, China*

*Corresponding author: guozhengkang@home.swjtu.edu.cn

Highlights

1. A 3D dislocation dynamics framework for various grain boundary (GB) types by using a 'coarse-graining' method was established.

2. The dislocation–GB interaction model considers both dislocation absorption and dislocation emission at GBs.

3. The compression behavior of several bicrystalline nanopillars with large-angle GB was investigated.

Abstract

Grain boundaries (GBs) have a significant influence on the mechanical properties of metallic materials. It has been a great challenge to describe dislocation interactions with various GBs. In the present article, a generalized dislocation–GB interaction model was constructed and then implemented in the three-dimensional multiscale discrete dislocation dynamics (DDD) framework. In the model, two dislocation–GB interaction mechanisms, i.e., dislocation absorption at GBs and dislocation emission from GBs, were considered. In order to make the dislocation–GB interaction model suitable for various GB types, a 'coarse-graining' approach was applied to deal with the process of dislocation absorption and emission. As the validations and applications of the proposed dislocation–GB interaction model, nanopillars containing a non-sigma large-angle GB and subjected to uniaxial compression were studied. The simulated results show that the bi-crystalline nanopillars possess a higher yield strength and

flow stress, smaller stress-drop size than single-crystalline counterparts, which is consistent with earlier experimental observations in the literature. Afterward, the DDD simulation was employed to reveal the effect of GB misorientation on the mechanical responses of bicrystals with a large-angle-symmetric-tilt GB. Simulations indicate that the mechanical responses of bicrystals are affected by the GB structures and complex dislocation–dislocation and dislocation–GB interactions. In contrast, the dislocation absorption and emission events, as well as the evolution of resolved shear stress and dislocation density, do not depend on the GB misorientation angles or the GB strength (or the GB energy).

1. Introduction

Grain boundaries (GBs) play a crucial role in the plastic deformation of polycrystalline materials, especially when the sample size is at the micro- or nano-scale. Different dislocation–GB interaction mechanisms may result in entirely distinct overall plastic deformation characteristics. Due to the variety of GB types and complicated GB structures, there are various interactions between dislocations and GBs, including dislocation transmission across GBs, dislocation absorption at GBs, and dislocation emission and reflection from GBs, as reviewed in Ref. [1]. In the past few decades, experimental observations [1], molecular dynamics simulations [2, 3] and phenomenological-constitutive-model-based finite element simulations [4, 5] have been utilized to investigate the properties of GBs and their effect on the mechanical behavior of materials.

Nowadays, discrete dislocation dynamics (DDD) simulation has become a versatile tool to investigate the plastic deformation of crystalline materials in the nano- and micro-sizes. DDD can be a bridge linking fundamental molecular dynamics studies and continuum models. Having the capacity to track the temporal and spatial evolution of dislocation networks, DDD simulation provides a possibility to establish the relationship among dislocation characteristics, plastic deformation mechanisms and mechanical properties.

The DDD approach has been used to study the effect of GB on bi-crystalline and polycrystalline materials. Early studies were mostly limited to two dimensional (2D) simulations and generally assumed that the GBs were impenetrable to dislocations [6-10]. Afterward, penetrable GB models accounting for dislocation transmission through GBs were developed and used to investigate the mechanical responses of polycrystals [11-16]. In 2009, Li et al. [11] proposed an energy-based penetrable GB model considering the effects of dislocation transmission across GBs and dislocation re-emission from GBs. Recently, Huang et al. [12] improved this dislocation–GB interaction model in a framework coupling 2D Discrete Dislocation Dynamics with Extended Finite Element Method (DDD–XFEM) by additionally considering the resolved shear stress on the potential outgoing slip planes and then used it to investigate the grain size effect and cyclic stress relaxation phenomena in polycrystalline aluminum. Moreover, to mimic the deformation behavior of nanocrystalline materials, Quek et al. [13, 14] proposed a dislocation–GB interaction model in a 2D DDD framework that incorporated dislocation transmission and GB sliding, absorption and emission at GBs. The 2D DDD studies have provided great insight into the plastic deformation and their relationship with dislocation–GB interaction mechanisms in polycrystalline materials. However, in the 2D DDD framework, the dislocations were 'pseudo point defects' and constrained to only up to 3 slip systems, which could not effectively capture the complex dislocation interactions such as cross-slip and junction [17, 18].

Three-dimensional (3-D) DDD can accurately model the evolution of dislocation structures and complicated short- and long-range interactions in sub-micron metallic materials. In the 3-D DDD framework, the dislocation is modeled as a line segment and moves under external stress in discrete time steps, producing more realistic dislocation microstructures. Up to date, there are very few studies using 3D DDD embedded with a dislocation–GB interaction model to probe the role of GB in the plastic deformation of polycrystalline or bi-crystalline materials. Jiang et al. [19] conducted 3D-DDD simulations on copper polycrystals to explore the effects of grain size and grain shape on the flow stress. However, the GB studied in [19] was treated

as a barrier and impenetrable to dislocation glide, which could not capture the features of GB. Thus, the 3D DDD embedded with a penetrable GB aroused considerable interest. For instance, Zhou et al. [17] performed a 3D DDD simulation to study the effects of film thickness and grain size on the strength of polycrystalline thin films. In that work, the process of dislocation transmission through GB was achieved by bowing out a Frank–Read (FR) source in outgoing grain when the resolved shear stress acting on the incoming dislocation exceeded the GB transmission strength. This model provided valuable insights for the influence of GB penetrability on the plastic deformation. However, the model assumed that there is no crystallographic change at a GB, i.e., the GB serves only to inhibit dislocation motion while the incoming and outgoing slip systems are identical. Recently, more comprehensive dislocation–GB interaction models have been proposed and developed. To name a few, Fan et al. [20] extended the 2D dislocation–GB interaction model proposed by Li et al. [11] to the 3D DDD framework. The dislocation–GB interaction model, as mentioned earlier, enables dislocation penetration through GBs and dislocation re-emission from GBs based on energy and geometric criteria, which was used to investigate the intermittent plastic deformation of micropillars under uniaxial compression [20] and the effect of GB on bi-crystalline materials under the nanoindentation [21]. Based on [20], Gao et al. [22] presented an improved model which introduces the terms of intrinsic stacking fault energy and unstable stacking fault energy into the energetic-condition-equations of dislocation penetration and emission. In addition, as a particular type of GBs, the twin boundary has also been modeled in the 3D DDD framework to study the effect of twin on the plasticity of face-centered cubic copper [23] and hexagonal close-packed magnesium [24, 25]. For small-angle symmetric tilt GBs (the misorientation between neighboring grains is less than 15°), the GB can be modeled by setting the specific energetic and geometric criteria for dislocation transmission and emission, as mentioned above. Some researchers [26, 27] treated the dislocation–GB interaction as the process of lattice dislocations of grain interior interacting with the pre-exited GB dislocations at GBs. It is noted that this method can only analyze

small-angle tilt GB that is comprised of a regular dislocation array, while cannot deal with other GB types that cannot be represented by specific dislocation array.

The penetrable GB models mentioned above have made significant success in studying the effect of GB on plasticity deformation. However, almost all these dislocation–GB interaction models are only suitable for small-angle symmetric tilt GBs. For such a GB type, the intersection lines of incoming and outgoing slip planes with the GB are coincident, making it convenient to deal with the transmission and emission processes of dislocation lines in the 3D DDD framework. Due to the variety of GB types, it is desirable and meaningful to develop a more generalized and physics-based dislocation–GB interaction model within the 3D DDD framework. In the present work, a 3D dislocation–GB interaction model that is suitable for various GB types and easy to be implemented in the polycrystalline DDD models is established by using a 'coarse-graining' method. The 'coarse-graining' scheme can capture the main features of dislocation–GB interactions without much loss of physical mechanisms and allows modeling the arbitrary crystallography, size, and geometry of the grain.

The paper is organized as follows. First, a concise description of the multiscale DD framework utilized in our simulations is given. Then a dislocation–GB interaction model based on a 'coarse-graining' approach is presented in detail. In flowing sections, the proposed dislocation–GB interaction model is validated and discussed: 1) Different compression responses between single- and bi- crystalline (containing a non-sigma large-angle GB) nanopillars; 2) The effect of GB misorientation on the bi-crystalline nanopillars containing large-angle symmetric tilt GBs. Finally, the paper concludes with a summary of the dislocation–GB interaction model and its application in bi-crystalline nanopillar compression, and the corresponding main findings are also presented.

2. Brief description of a multiscale DDD framework

A hybrid model (multiscale DDD model) [21, 28-30], which couples discrete dislocation dynamics (DDD) with finite element method (FEM), is employed to

implant a dislocation–GB interaction model and then conduct simulations. This multiscale DDD framework is originally developed by Zbib et al. [28, 29] and recently improved by Huang et al. [30]. In this model, the plastic strain obtained from the DDD is coarse-grained to the FEM, thus releasing the discontinuities of plastic strain and stress field among adjacent elements. Besides, a stress correction is introduced in the dislocation stress filed to address the underestimated stress between two close dislocation segments faced in traditional DDD–FEM coupling frameworks. The detail of this hybrid DDD–FEM model can be referred to Refs. [21, 30, 31].

3. Grain boundary model

As mentioned in Section 1, it is desirable to establish a versatile dislocation–GB interaction model within the framework of 3D DDD. In the present article, we construct a dislocation–GB interaction model applicable for various GB types and convenient to be incorporated in polycrystalline models.
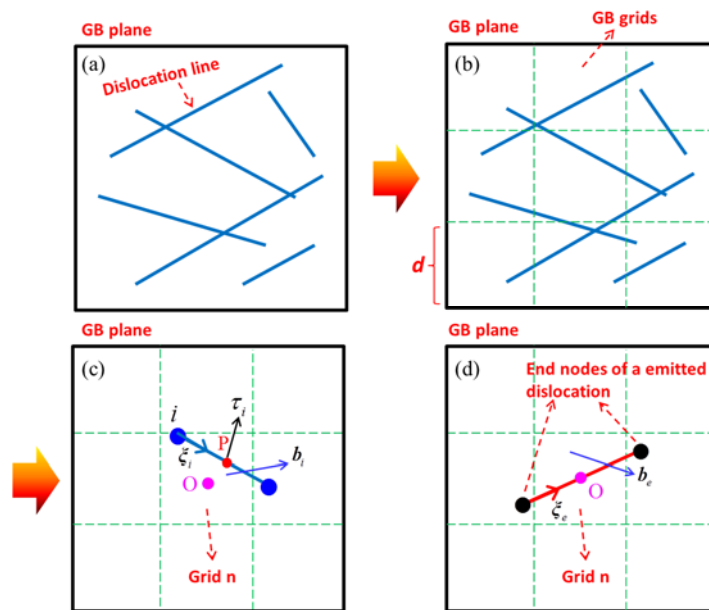

Fig. 1. (a) Schematic of pile-up dislocation lines at the grain boundary (GB) plane; (b) The GB is divided into several grids with equal size of d to deal with the dislocation absorption at GBs and dislocation emission from GBs. Each grid can be envisaged as a dislocation sink for dislocation absorption and a dislocation source for dislocation emission; (c) Schematic of dislocation segment i absorbed in grid n; (d) Grid n emits a dislocation source with its midpoint coinciding with the center of the grid.

As shown in Fig. 1a, for a non-symmetric-tilt-GB, the pile-up dislocations at the GB are irregular since the intersection lines of two slip planes of neighboring grains at the GB usually do not coincide with each other. Thus, it is difficult to deal with the transmission of dislocation lines in the DDD framework. To overcome this difficulty, a 'coarse-graining' method was used to handle the transmission of dislocations across the GB with an arbitrary GB type. Two dislocation–GB interaction mechanisms, i.e., dislocation absorption at GBs and dislocation emission from GBs, were considered.

3.1 Dislocation absorption at GBs

When a dislocation approaches the GB, it will stop moving forward due to the resistance of the GB. However, when the resolved shear stress acting on dislocation reaches the GB strength, the dislocation will be absorbed by the GB. The critical stress for dislocation absorption, τ_C, can be determined by the following equation:

$$\tau_C = E_{GB} / b , \tag{1}$$

where b is the magnitude of the Burgers vector, and E_{GB} is the GB energy. The GB energy is related to different GB structures and can be determined through molecular dynamics simulations.

After absorption, the dislocation node of the lattice dislocation connected with the GB becomes a 'GB node'. Note that the GB is envisaged as an area with severe lattice distortion and does not like the free surface where the dislocations can annihilate or move freely. The GB nodes are not allowed to annihilate at the GB and can only move along the intersection line of the slip plane and GB. The velocity of the GB node, v_{GN}, is determined as follows:

$$v_{GN} = \frac{f_{effective}}{B} \left[(\boldsymbol{\xi} \times \boldsymbol{n}) \cdot (\boldsymbol{n} \times \boldsymbol{n}_{GB}) \right] (\boldsymbol{n} \times \boldsymbol{n}_{GB}), \tag{2}$$

where B is the viscous drag coefficient, $f_{effective}$ is the effective force contributing to the movement of dislocations along the intersection line of the slip plane and GB $\boldsymbol{n} \times \boldsymbol{n}_{GB}$, where $\boldsymbol{n}$ and $\boldsymbol{n}_{GB}$ are their normal unit directions. The effective force is determined by

$$f_{\text{effective}} = \left[\boldsymbol{F}_{\text{GN}} \cdot \left(\boldsymbol{\xi} \times \boldsymbol{n} \right) \right] - f_{\text{GN}}, \tag{3}$$

where $\boldsymbol{F}_{\text{GN}}$ is the total external force experienced by the to be absorbed dislocation segment with unit line direction $\boldsymbol{\xi}$. f_{GN} denotes the lattice friction of GB nodes and set to be larger than that of free surface dislocation nodes or lattice dislocation nodes (in the present work, the lattice friction of these nodes is set as zero), since the resistance for dislocation nodes to glide is higher for GB surfaces than free surfaces. It should be noted that $v_{\text{GN}} = 0$ if $f_{\text{effective}} < 0$ in Eq. (2).

In order to deal with the situation that multiple dislocation segments are absorbed at GBs, a 'coarse-graining' method is applied to handle the irregular absorbed dislocation lines. As shown in Fig. 1b, the GB is divided into several grids with an equal size of d. Each grid can be envisaged as a dislocation sink. As shown in Fig. 1c, if the effective shear stress τ_i of a dislocation segment i exceeds the critical value τ_c determined by Eq. (1), the segment i will be absorbed in the GB grid n (the coordinate of segment's midpoint P locates in grid n). The Burgers vector, length and line direction of 'GB dislocations' in the GB grid n are the sums of all absorbed dislocation segments in this grid:

$$\boldsymbol{b}_{\text{GB}}^{n} = \sum \boldsymbol{b}_i, \quad l_{\text{GB}}^{n} = \left| \sum \boldsymbol{l}_i \right|, \quad \boldsymbol{\xi}_{\text{GB}}^{n} = \sum \boldsymbol{\xi}_i. \tag{4}$$

3.2 Dislocation emission from GBs

With the increasing number of absorption events, more and more dislocations will be stored at GBs. The GB becomes unstable when the energy of GBs increases to a certain degree. Therefore, the emission of dislocations from GBs is introduced to reduce the GB energy. Similar to the case of dislocation absorption at GBs, the 'coarse-graining' method is also used to deal with the emission of dislocations from GBs. The GB grid can be envisaged as a source of dislocation emission. The emitting events are determined by the following rules.

(1) Emitting grain: the GB dislocations emit to the grain with a smaller total length of absorbed dislocation segments. For example, suppose that the total lengths of dislocations absorbed at GB from grain 1 and grain 2 (grain 1 and grain 2 are

grains at two sides of a GB) at the GB grid n are l_1 and l_2, respectively. If $l_1 > l_2$, the GB dislocations will emit to grain 2 and vice versa.

(2) Slip plane of the emitting dislocations: assume that the line direction of the intersection line of an emitting slip plane with the GB is $\boldsymbol{\xi}_e$, then the slip plane of emitting dislocations can be determined by rendering the absolute value of $\boldsymbol{\xi}_e \cdot \boldsymbol{\xi}_{GB}^n$ be minimum.

(3) Burgers vector of emitting dislocations: after determining the grain and slip plane of an emitting dislocation, there are three candidate Burgers vectors to select. In the current dislocation–GB interaction model, the same method used in Refs. [11, 20] is adopted to determine the emitting dislocation's Burgers vector, i.e., the residual Burgers vector, $\boldsymbol{b}_r = \boldsymbol{b}_{GB} - \boldsymbol{b}_e$ (where $\boldsymbol{b}_e$ is the Burgers vector of the emitting dislocation), of GB dislocations after emitting, should be minimum. This rule ensures that the emitting process is energetically favorable.

(4) Length of emitting dislocations: the length of an emitting dislocation is l_{GB}^n as expressed in Eq. (4).

(5) Line direction of emitting dislocations: there are two possible line directions of an emitting dislocation line; the line direction is chosen to make the emitting dislocation move toward the grain interior (the moving direction of a dislocation segment is related to its line direction and its Burgers vector).

(6) Characteristics of emitting dislocations' end nodes: similar to the GB nodes mentioned in Section 3.1, the motions of an emitting dislocation's two end nodes are constrained in the intersection line of the slip plane and GB. Besides, the velocity, $\boldsymbol{v}_{EN}$, of an emitting dislocation's end node also has a similar expression as Eq. (2):

$$\boldsymbol{v}_{EN} = \frac{f_{\text{effective}}}{B} \left[\left(\boldsymbol{\xi} \times \boldsymbol{n} \right) \cdot \left(\boldsymbol{n}_{GB} \times \boldsymbol{n} \right) \right] \left(\boldsymbol{n}_{GB} \times \boldsymbol{n} \right), \tag{5}$$

with

$$f_{\text{effective}} = \left[\boldsymbol{F}_{EN} \cdot \left(\boldsymbol{\xi} \times \boldsymbol{n} \right) \right] - f_{EN}, \tag{6}$$

where $\boldsymbol{F}_{EN}$ is the total external force acting on the dislocation segment. f_{EN} is the friction of emitting dislocations' end nodes and set to be larger than that of lattice

dislocation nodes. In addition, similar to the case of dislocation absorption at GBs, v_{EN} = 0 when $f_{effective}$ <0 in Eq. (5).

In addition to the six emitting rules listed above, the emitting dislocations also need to satisfy critical stress conditions. The critical activation stress τ_e for a Frank–Read (FR) source can be calculated using equation [32, 33]:

$$\tau_e = \frac{A}{2\pi} \frac{\mu b}{l_e} \log \frac{l_e}{r}, \tag{7}$$

where μ is the shear modulus of materials, l_e is the length of the emitting dislocation. A is the parameter depending on dislocation types: A equals 1 for edge dislocations while $1/(1-\nu)$ (with ν being the Poisson's ratio) for screw dislocations. In the simulations, there are different types of dislocations (including edge, screw and mixed ones), so the parameter A is approximated through the rule of mixture as $A=[1+1/(1-\nu)]/2$. The parameter r is the Brown splitting distance and is usually set as $2b$ [33].

Once the dislocation absorption in grid n occurs, the program will check whether the emitting events can happen in the following time steps of DDD calculations. When the candidate emitting dislocations satisfy the emitting criteria (1)–(6) and critical stress condition in Eq. (7) simultaneously, the GB grid n will emit a lattice dislocation into the corresponding grain with its midpoint at the center of the grid, as shown in Fig. 1d. After emitting, the Burgers vector, length and line direction of GB dislocation for grid n become zero, i.e., $\boldsymbol{b}_{GB}^n = 0$, $l_{GB}^n = 0$, $\boldsymbol{\xi}_{GB}^n = 0$. This treatment is mainly based on the assumption that the energy of absorbed dislocations at GBs is completely released when the emission events occur. In each DDD time step, only one emitting event can occur for each GB grid.

Note that although the dislocation–GB interactions described in Section 3.1 and Section 3.2 may not totally take the precise and detailed configuration of dislocations into account, the present dislocation–GB interaction model is applicable for symmetric and non-symmetric GBs and can capture many important features of the effect of GBs on the deformation of bicrystals or polycrystals. It should also be

mentioned that the GB structure in real metallic materials is very complicated, which may not be fully represented by the present GB model. However, this GB model can capture some main features of a GB to a certain extent. The GB structure reflected by this GB model can be regarded as the structure induced by the non-coincidence of crystallographic orientations and slip systems of two grains at the GB surface. The further analysis and validation of the present dislocation–GB interaction model will be presented in the following sections.

4. Validation of the dislocation–GB interaction model

4.1 Compression of single- and bi- crystalline nanopillars

As the validation and application of the present dislocation–GB interaction model, the deformation behavior of a bi-crystalline nanopillar and its single-crystalline counterparts under uniaxial compression is investigated.
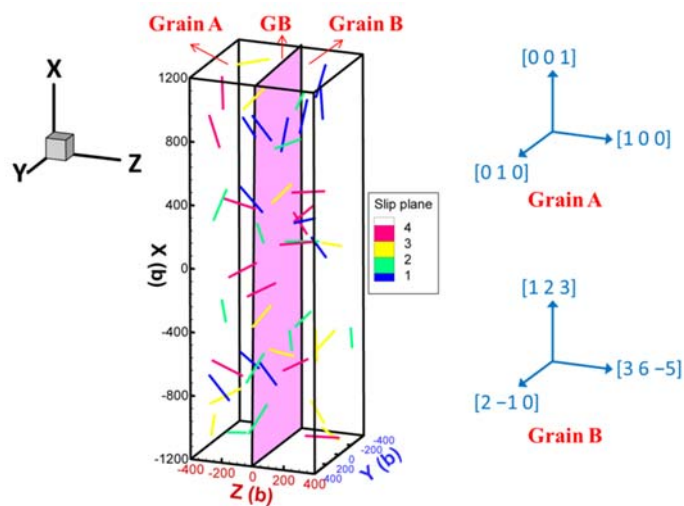

Fig. 2. Geometry and crystallographic orientations of the bi-crystalline nanopillar. The compression directions and GB normal directions of bicrystalline components, Grain A and Grain B, are along with the crystallographic orientations of [0 0 1], [1 2 3] and [1 0 0], [3 6 $\bar{5}$], respectively.

The geometry and crystallographic orientations of the bi-crystalline nanopillar in present simulations are shown in Fig. 2. The height-to-width ratio of the sample is chosen as 3, which is often used in previous experimental studies of nanopillar compression [34-38]. In current simulations, the width of the sample is set as w=800 b, where b is the magnitude of the Burgers vector. The GB is located in the middle of the sample and parallel to the Z-surface (see Fig. 2). As shown in Fig. 2, the bicrystals consists of two single crystals, Grain A and Grain B, with the compression directions and GB normal directions aligned with the crystallographic orientations of [0 0 1], [1 2 3] and [1 0 0], [3 6 $\bar{5}$], respectively. The misorientation between the two grains is 45.5° around [$\bar{1}$ $\bar{4}$ 3]. To examine the effect of GB, two single-crystals with the same orientation as the bicrystals, i.e., the [0 0 1]-oriented grain A and [1 2 3]-oriented grain B, were also simulated for comparison. The geometry and size of the single crystalline pillars are identical with that of bicrystals. It should be noted that the compression orientation may have a significant effect on the mechanical responses of the single- and bi-crystals due to the difference of dislocation activation on slip systems. Table 1 lists the Schmid factor of the [0 0 1]-oriented and [1 2 3]-oriented single crystals. It can be seen that the [0 0 1]-oriented single crystal has eight slip systems with the same Schmid factor of 0.408, which implies that multiple slips will occur during deformation. In contrast, the [1 2 3]-oriented single crystal is oriented for a single slip, as it only has one slip system possessing the highest Schmid factor of 0.467.

Table 1. Slip systems and their Schmid factors in [001]-oriented and [123]-oriented single crystals

Label	Slip systems	Schmid factor [001] orientation	Schmid factor [123] orientation
1	(1 $\bar{1}$ 1)[1 0 $\bar{1}$]	0.408	0.117
2	(1 $\bar{1}$ 1)[0 $\bar{1}$ $\bar{1}$]	0.408	0.292
3	(1 $\bar{1}$ 1)[$\bar{1}$ $\bar{1}$ 0]	0.000	0.175
4	($\bar{1}$ 1 1)[0 1 $\bar{1}$]	0.408	0.117
5	($\bar{1}$ 1 1)[$\bar{1}$ 0 $\bar{1}$]	0.408	0.467
6	($\bar{1}$ 1 1)[$\bar{1}$ $\bar{1}$ 0]	0.000	0.350
7	($\bar{1}$ $\bar{1}$ 1)[$\bar{1}$ 1 0]	0.000	0.000
8	($\bar{1}$ $\bar{1}$ 1)[$\bar{1}$ 0 $\bar{1}$]	0.408	0.000
9	($\bar{1}$ $\bar{1}$ 1)[0 $\bar{1}$ $\bar{1}$]	0.408	0.000

10	(1 1 1)[$\bar{1}$ 1 0]	0.000	0.175
11	(1 1 1)[0 1 $\bar{1}$]	0.408	0.175
12	(1 1 1)[1 0 $\bar{1}$]	0.408	0.350

The material simulated in this paper was taken to be isotropic elastic aluminum; the associated material constants, as well as the GB parameters, are listed in Table 2. In order to determine the GB energy of this specific GB type, molecular dynamics simulations were carried out using the method presented in Ref. [39]. The calculated GB energy is 478.3 mJ/m^2. Note that both f_{GN} in Eq. (3) and f_{EN} in Eq. (6) are set to be equal to the shear modulus μ. This treatment implies that the GB nodes connected with the GB after dislocation segments absorption at GBs and the two end nodes of the emitting dislocation cannot move during the loading, which can be regarded as a pinned point like the two ends of a FR source.

Table 2. Parameters of aluminum and grain boundary used in simulations.

Material parameters	Symbol	Value
Density (kg/m^3)	ρ	2700
Shear modulus (GPa)	G	26
Poisson's ratio	v	0.345
Burgers vector magnitude (nm)	b	0.25
Viscous drag coefficient (Pa·s)	B	10^{-4}
Grain boundary (GB) parameter (GPa·b)	f_{GN}, f_{EN}	26
GB grid size (b)	d	100

The bottom surface of the sample is fully constrained, and the top surface is uniaxially compressed along the X-direction in a displacement-controlled mode, with a constant strain rate of 5000 s^{-1}. FR sources with a fixed length of 200 b are randomly distributed in the pillars. The initial dislocation lines are not allowed to intersect the GB in the bi-crystalline samples. All twelve slip systems of the FCC crystal are taken into account, with each slip system having four sources (in the bi-crystalline pillar, there are two sources in each slip system in both grains), resulting in an initial dislocation density of 100 μm^{-2}. A bi-crystalline pillar containing a rigid GB, which acts as a barrier and prohibits dislocations from penetrating the GB, was also simulated to examine the influence of GB penetrability on the mechanical

behavior. Since the positions of FR sources are distributed randomly, each result was achieved by averaging eight realizations with different FR source distributions.

Fig. 3a presents the compressive stress–strain curves of single-crystal A (S-A), single-crystal B (S-B), bicrystals with rigid GB (B-RGB), and penetrable GB (B-PGB). It can be seen from Fig. 3a that the flow stress and strain hardening rate of B-RGB are significantly higher than that of B-PGB. The larger stress of B-RGB is related to the dislocation pill-ups in front of GBs. Due to the blocking effect of a rigid GB, the dislocation accumulation at the vicinity of GBs gradually increases with increasing loading strain. Hence, as shown in Fig. 3b, the dislocation density of B-RGB increases significantly as the strain increases. As a result, the severe mutual interaction of dislocations at GB and the lack of sufficient mobile dislocations in the grain interior lead to increased flow stress and a high hardening rate in B-RGB cases. On the contrary, if the mechanisms of dislocation absorption at GBs and dislocation emission from GBs are taken into account, the flow stress is greatly reduced, as the B-PGB case shown in Fig. 3a. Interestingly, the B-PGB pillars initially yield at point A and harden to point B with a similar hardening rate as the B-RGB case; after that, B-PGB immediately enters a stage of ideal plasticity where the flow stress level remains unchanged with increasing strain. Fig. 3c plots the emitted dislocation density of B-PGB as a function of strain; the corresponding stress and total dislocation density are also presented in this figure. It shows that the total dislocation density starts to increase from point A, indicating the dislocations begin to activate and the B-PGB yields. With further loading, more and more dislocations are blocked in front of GB, the stress acting on dislocations in the frontier of the pile-up reaches the GB strength, and then the leading pile-ups are absorbed by the GB. When the emission criteria (described in Section 3.2) are met, dislocation emission from GBs occurs, the emitted dislocation density starts to increase with increasing strain, as indicated by point B in Fig. 3c. At the same time, the flow stress of B-PGB immediately enters a state of ideal plasticity and deviates from the case of B-RGB (see point B in Fig. 3a). This is because the emitted dislocations can release the stress concentration at GBs and provide more mobile dislocations to accommodate further plastic deformation. It can

also be seen from Fig. 3c that the increasing rates of total and emitted dislocation densities are nearly the same, suggesting that the emitted dislocations play a dominant role in the deformation and mechanical response of B-PGB after point B.
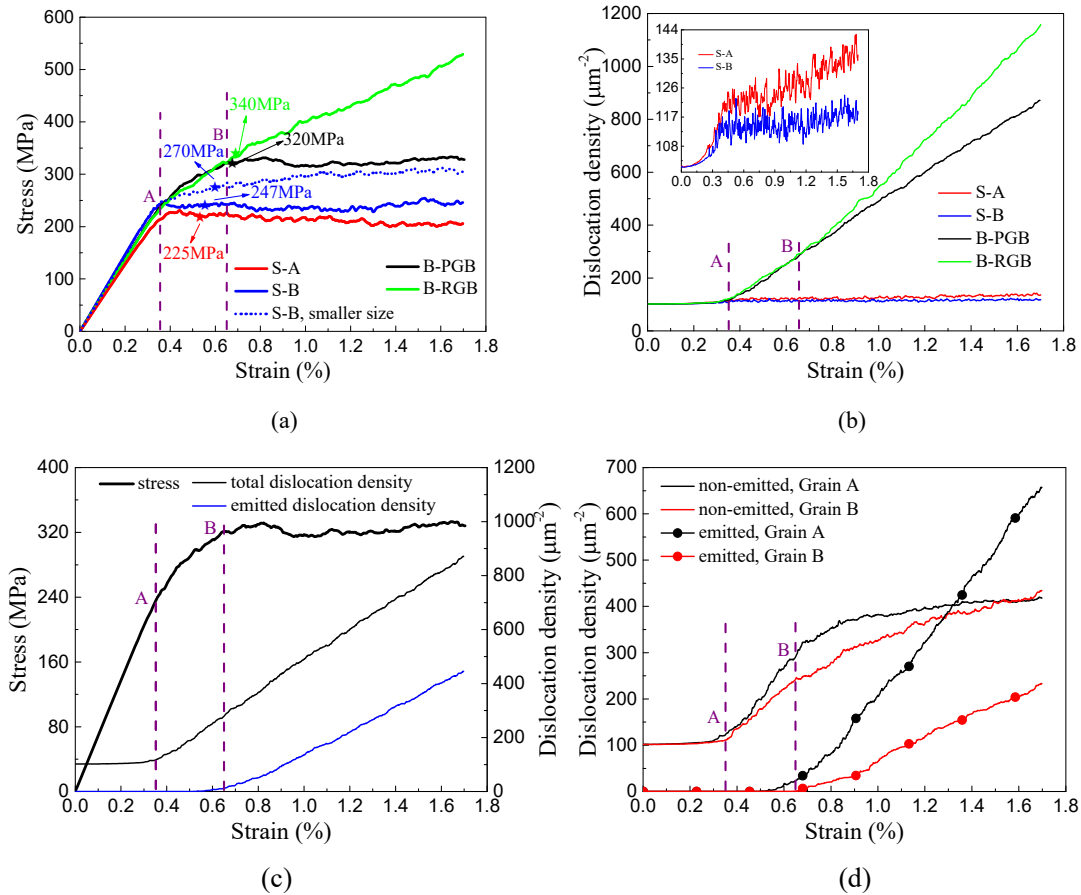

Fig. 3. (a) Compressive engineering stress–strain curves and (b) dislocation density versus strain of single-crystal A (S-A), single-crystal B (S-B), bicrystals with rigid GB (B-RGB) and penetrable GB (B-PGB). (c) Evolution of stress, emitted dislocation density and total dislocation density of B-PGB. (d) The density of emitted and non-emitted dislocation versus strain for Grain A and Grain B in B-PGB. The curve of the single-crystalline pillar with the same orientation but half-size as S-B is also plotted in (a). The solid star symbols marked in (a) represent the yield points taken from the plastic strain of 0.2%. The inset in (b) shows the enlarged dislocation density versus strain curves of S-A and S-B. Point A and point B (purple dash lines) in subfigures a–d represent the start of yielding and dislocation emission from GB in B-PGB.

As displayed in Fig. 3a, the single-crystal A (S-A) has a slightly lower yield and flow stress than that of single-crystal B (S-B). According to the Schmidt law, the

compressive stress needed for activation of slip systems with the highest Schmid factor of 0.408 in S-A should be higher than that needed for slip systems with the highest Schmid factor of 0.467 in S-B. This contradiction is attributed to the dislocation activations. There are eight slip systems sharing the highest Schmid factor in S-A, while the S-B only has one slip system with the highest Schmid factor. Therefore, the number of potential dislocations to be activated and multiplied in S-B is much smaller than that in S-A. Hence, the first dislocation activation to yield the pillar for S-A is easier, leading to lower compressive yield stress. In order to further examine the difference of dislocation activation and motion in these two single-crystalline pillars, Fig. 4 shows the percentage of the contribution of dislocation motion in each slip system to the whole plastic strain of the pillars during plastic deformation. As can be seen in Fig. 4, there are eight slip systems that contribute to the whole plastic deformation in S-A, while there are only three slip systems that are activated and contribute to the deformation of S-B. The dislocation density during the plastic deformation of S-A is higher than S-B, as shown in the inset of Fig. 3b. Again, this is because there are more slip systems available to operate the dislocations in S-A, thus leading to a higher dislocation density than that of S-B. As for the S-B sample, it is interesting to see that the dislocation sources are first activated in the slip system with the highest Schmid factor of m=0.456, and then the dislocations in another two slip systems with the second-highest Schmid factor of m=0.350 are gradually triggered to accommodate an increasing plastic deformation. The contribution percentages of these slip systems gradually reach a steady value at an engineering strain around 1.1% and then keep stable until the end of loading (as seen in Fig. 4b). Additionally, the S-A case shows that the contribution percentages of eight equivalent slip systems with an identical Schmid factor of m=0.408 are not the same (see Fig. 4a), although the values are obtained by averaging eight realizations. This phenomenon is mainly caused by the strong stochastic nature of crystalline materials at small scale. Fig. 3d presents the density variation of emitted and non-emitted dislocations in Grain A and Grain B, as a function of strain, for the case of B-PGB. It can be seen that the density of emitted dislocation in Grain A is much

higher than that of Grain B. This can be attributed to the following aspect: As shown in Fig. 3a, the abrupt elastic-plastic transition point of S-B occurs at an engineering strain of about 0.35%, which is 0.05% smaller than that of S-A. This implies that the first dislocation activation to yield the material in Grain B will be earlier than that of Grain A for the B-PGB samples. Therefore, a larger number of dislocations from Grain B are piled up near the GB and then absorbed by the GB, resulting in more dislocations emitted to adjacent grain (Grain A). This process can be envisaged as a dislocation 'transmission' (absorbed then emitted) through the GB.
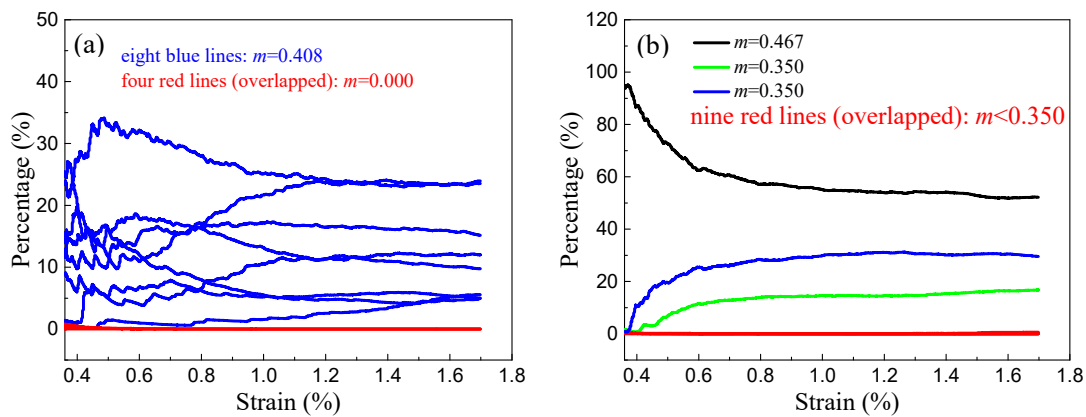

Fig. 4. Percentage of the contribution of each slip system to the whole plastic strain of the pillars during plastic deformation. (a) Single-crystal A (S-A) and (b) Single-crystal B (S-B). The Schmid factor m of 12 slip systems for S-A ([0 0 1]-oriented) and S-B ([1 2 3]-oriented) are listed in Table 1.

The elastic moduli for S-A, S-B and B-PGB obtained from Fig. 3a are E_{S-A}=63.88 GPa, E_{S-B}=73.17 GPa and E_{B-PGB}=68.59 GPa, respectively. As expected, the elastic modulus of the bi-crystalline pillar lies between its component single-crystalline ones and approximately follows the rule of mixture, i.e., $E_{B-PGB} \approx (E_{S-A} + E_{S-B})/2$. Fig. 3a also shows that the yield stress $\sigma_{0.2}$ defined as the stress at a plastic strain of 0.2% in B-PGB ($\sigma_{0.2}$=320 MPa) is higher than that in its single-crystalline components, S-A ($\sigma_{0.2}$=225 MPa) and S-B ($\sigma_{0.2}$=247 MPa). This result is in good agreement with experimental observations reported in the literature [34, 40-44]. Most of the experimental studies [34, 40] mainly attributed the hardening

and higher strength of bi-crystalline pillars to the reduction of dislocation length in the component grains resulting from the dislocation obstruction by GB (each grain in a bi-crystal is half of the single- or bi-crystalline pillar size). However, as mentioned above, in this simulation, the hardening stage from point A to point B in Fig. 3a is mainly attributed to the dislocation pile-up in front of GB. However, this does not mean that the effect of dislocation obstruction by GB has been excluded. Ng and Ngan [41] conducted compression experiments on bi-crystalline Al pillars with a large-angle GB and found severe dislocation accumulation near the GB. They pointed out that the higher strength in a bi-crystal was mainly due to the significant dislocation pile-ups at GBs, although the smaller size of the two constituent grains (compared with that of single-crystalline pillars) might also partially contribute to the higher flow stress. In order to clarify this issue, A single-crystalline pillar having the same orientation as S-B ([1 2 3]-oriented) but with only half the size of the bi-crystalline pillars is simulated. The dimensions of this sample in X, Y and Z directions are $2400b$, $800b$ and $400b$, respectively. The initial FR source length, dislocation density and other simulation set-ups keep the same as that used in S-B. The simulated stress–strain curve for this smaller single-crystalline pillar is plotted in Fig. 3a. It clearly shows that the yield strength $\sigma_{0.2}$, as well the following flow stress of this smaller S-B lies between the cases of B-PGB and larger S-B. This indicates that the hardening induced by both the dislocation accumulation behind the GB and size effect from the reduced volume in each grain of B-PGB pillars is responsible for the higher flow stress of B-PGB compared with its same-sized single-crystalline counterparts. This conclusion is consistent with Ng and Ngan's experiments [41].

Dislocation networks for S-A, S-B, B-RGB and B-PGB at a total engineering strain of 1.2% are presented in Fig. 5a. It shows that there is no dislocation accumulation in the cases of S-A and S-B since the dislocations can sweep through the whole sample and annihilate at the surfaces freely for the single-crystalline pillars. In contrast, the B-RGB pillar, which contains a rigid GB, has substantial dislocations, from both Grain A and Grain B, piling up in the vicinity of GB. However, in the

B-PGB case, where the dislocation absorption and emission are considered, the dislocation accumulation in front of GB is reduced. To examine the dislocation distribution quantitatively, the distributions of the total dislocation density along the Z-axis (the normal direction of the GB) for single- and bi- crystalline pillars are plotted, as shown in Fig. 5b. The whole sample was divided into 16 slabs in the Z direction, and then the average of dislocation density in each slab was calculated. It can be seen from the figure that the dislocation density does not change along Z-axis for single crystal, whereas there is a peak dislocation density at GB for the bi-crystalline ones. It should be noted that the total dislocation density of B-PGB increases intensively with increasing strain after point B (see Fig. 3b). According to the Taylor hardening mechanism, the strength will rise in proportion to the square root of dislocation density. However, the flow stress of B-PGB still keeps at a constant level with increasing strain, as shown in Fig. 3a. This is because the high total dislocation density in B-PGB is mainly composed of emitted dislocations. The emitted dislocations can operate into the grain interior and then generate plastic strain, which may greatly compensate for the increment of strength that comes from the forest hardening of dense dislocations, leading to an overall response of ideal plasticity as shown in Fig. 3a. Fig. 5b also supports this argument. As observed from this figure, there are comparable values of total dislocation density at the position of GB ($Z=0$) for B-RGB and B-PGB. However, for the case of B-RGB, the dislocation accumulation at GB consists of pilling up dislocations, which are immobile and thus induce high back stress to inhibit further dislocation motion in the grains, contributing to a significantly high work-hardening rate. While there are a large number of emitted dislocations (red dislocation lines in Fig. 5a) residing near the GB in the B-PGB pillar. The emission events can provide more mobile dislocations and contribute to the softening of the pillar, resulting in the absence of strain hardening in the case of B-PGB after point B (see Fig. 3a).
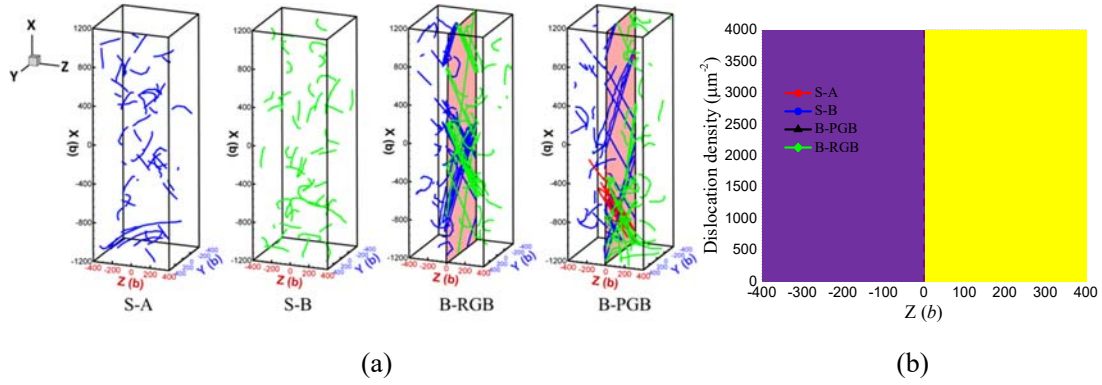
Fig. 5. (a) Representative dislocation structure at 1.2% straining for S-A, S-B, B-RGB and B-PGB samples. The blue and green dislocation lines in B-RGB and B-PGB represent the dislocations at Grain A (left grain) and Grain B (right grain), respectively, the red lines in B-PGB are the emitted dislocations. (b) Dislocation density distribution along the *Z*-axis for four types of pillars.

The stress–strain curves of the micron- or nano-sized crystalline pillar is jumpy and stochastic. The stress–strain curves exhibit strain bursts under the load-controlled manner, while stress drops will be observed in a displacement-controlled mode, as investigated in the present work [45, 46]. Fig. 6 presents the stress drop number versus stress drop size for four types of pillars. Here, we define the stress drops with size larger than 20 MPa ($\Delta\sigma$>20 MPa), between 10 MPa and 20 MPa (10 MPa<$\Delta\sigma$<20 MPa), and smaller than 10 MPa ($\Delta\sigma$<10 MPa) as large, medium, and small stress drops, respectively. It can be found that the number of large and medium stress drops in the pillars is S-B > S-A > B-PGB > B-RGB.

The stress drops $\Delta\sigma$ in micropillar can be qualitatively explained according to Hook's law

$$\Delta\sigma = E\left(\Delta\varepsilon - \Delta\varepsilon^{\mathrm{p}}\right), \tag{8}$$

where $\Delta\varepsilon$ and $\Delta\varepsilon^{\mathrm{p}}$ are the external and plastic strain increment of pillars for a DDD step, respectively. As seen from Eq. (8), when $\Delta\varepsilon^{\mathrm{p}}$ is larger than $\Delta\varepsilon$, the stress drop occurs ($\Delta\sigma$ becomes negative). A larger plastic strain increment in a DDD step will result in a larger stress drop. The plastic strain comes from the movement of dislocations, and the average moving distance in a DDD's simulation step can be approximated to be the dislocation mean free path (MFP). This implies

that the larger MFP will generate a larger plastic strain during a time step, thus leading to a larger stress drop. The MFP λ consists of contributions due to GB and forest dislocations in a harmonic way as [47, 48]

$$\frac{1}{\lambda} \approx \frac{\sqrt{\rho_f}}{k_f} + \frac{1}{k_{GB}d} , \qquad (9)$$

where ρ_f is the forest dislocation density, d is the grain size, k_1 and k_2 characterize the obstacle strength of forest dislocations and GB, respectively. It is noted that GB is a stronger obstacle comparing with forest dislocations, thus $k_f > k_{GB}$.

In the sing-crystalline pillars, there are eight slip systems activate during the plastic deformation in S-A, while the S-B only has three slip systems to operate, as shown in Fig. 4. This suggests that there will be stronger dislocation interactions in the S-A pillar, leading to a higher forest dislocation density and a smaller MFP for dislocation gliding. While for the case of S-B, due to a lower probability of dislocation interaction with each other, the activated dislocations can move with a larger MFP in each intermittent operation. Moreover, the relatively higher dislocation density of S-A compared to the case of S-B shown in the inset of Fig. 3b also manifests that the MFP for dislocation gliding in S-A is smaller than in S-B. A larger MFP means that dislocations can sweep a larger area and create a larger plastic strain increment. Thus, large and medium stress drops in S-B are more than that in S-A.

Compared with the single-crystalline pillars, the stress drop sizes in bi-crystalline pillars are smaller. The phenomenon of smaller stress drops in bi-crystals is consistent with experimental findings [34, 35, 41] and previous three-dimensional DDD study [20]. Theoretically, smaller stress drops have a relationship with the smaller MFP. According to Eq. (9), the MFPs of dislocations in bi-crystalline pillars are reduced owing to the impeding and truncating effects of GB on dislocation gliding. Such impeding effects are larger in B-RGB than that in B-PGB; thus, it gives $k_{PGB} > k_{RGB}$ and $\lambda_{PGB} > \lambda_{RGB}$ according to Eq. (9). Moreover, in contrast to the absence of

dislocation emission in B-RGB, the emitting event in B-PGB can also generate a relatively large stress drop. Thus, B-PGB has more large and medium stress drops than B-RGB.
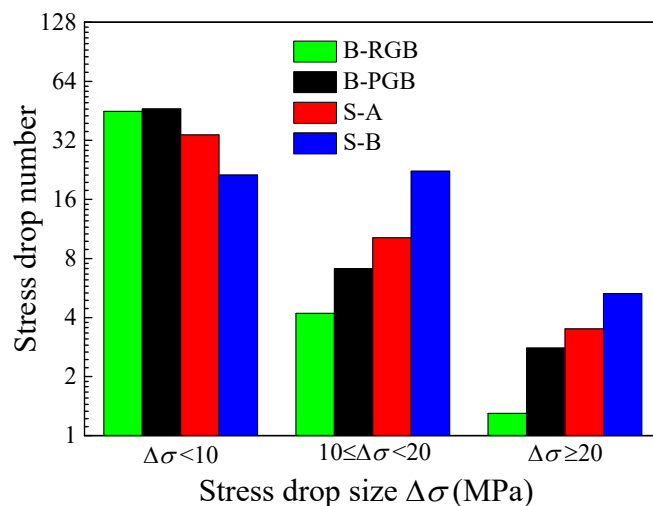

Fig. 6. Stress drop number versus drop size for S-A, S-B, B-RGB and B-PGB samples in the whole deformation.

4.2 Effect of GB misorientation on bi-crystalline nanopillars

In this section, compression simulations on three bi-crystalline nanopillars containing large-angle symmetric tilt GBs with different misorientation angles (θ) around the [1 $\bar{1}$ 0] tilt axis are conducted to validate the present dislocation–GB interaction model further. The geometry and dimension of the bi-crystalline pillars are the same as the pillar in Section 4.1 (see Fig. 2). The GB's [1 $\bar{1}$ 0] tilt axis of three studied bicrystals, i.e., bicrystals A (B-A), bicrystals B (B-B) and bicrystals C (B-C), are aligned with the *Y*-axis. It means that the loading direction in *X*-axis is perpendicular to the [1 $\bar{1}$ 0] tilt axis (see Fig. 2). This set-up has also been adopted in MD simulations to investigate the effect of GB on the mechanical response of bi-crystals [49-53]. The GBs of three bicrystals, together with corresponding misorientation angle, GB energy γ_{GB} (taken from Ref. [49]) and GB strength τ_{GB} ($\tau_{GB}=\gamma_{GB}/b$) are listed in Table 3. Note that two constituent grains in bicrystals have the same highest Schmid factor to the loading direction. The highest Schmid factors of three samples are also summarized in Table 3. The initial Frank–Read source length

and dislocation density in three pillars here are identical with the bi-crystalline pillar investigated in Section 4.1.

Table 3. Summary information of [1 $\bar{1}$ 0] symmetric tilt grain boundaries in bicrystals A (B-A), bicrystals B (B-B) and bicrystals C (B-C).

Samples	GB Σ (h k l)	Misorientation angle (°)	GB energy γ_{GB} (mJ/m^2)	GB strength τ_{GB} (MPa)	Schmid factor m	Yield stress σ_y (MPa)
B-A	Σ19{1 1 6}	26.5°	406.3	1625.2	0.430	328
B-B	Σ139{3 3 11}	42.2°	319	1276	0.399	352
B-C	Σ33{2 2 5}	58.9°	300	1200	0.334	425

The engineering stress–strain curves of three bicrystals are depicted in Fig. 7a. The yield stresses taken from the flow stresses at 0.2% plastic strain for B-A, B-B and B-C are 328 MPa, 352 MPa and 425 MPa, respectively; these values are also listed in Table 3. From Table 3 and Fig. 7a, it can be seen that the yield stress, as well as the flow stress after yielding, increases as the GB's misorientation angle increases. This result qualitatively agrees with previous studies using molecular dynamics simulations [50, 54]. However, this does not mean that the difference in yield stress solely comes from the effect of GB misorientation since the highest Schmid factors of three samples are different. To eliminate this influence, the resolved shear stresses, which are calculated by multiplying the stresses in Fig. 7a by the corresponding highest Schmid factors. Fig. 7b displays the relationship between resolved shear stress and plastic strain. It shows that the resolved shear stresses of three bicrystals are nearly the same at a plastic strain of ~0.1%. With further loading, the resolved shear stress of B-C starts to be significantly lower than that of B-A and B-B, especially when the plastic strain is larger than ~0.3%. Also, Fig. 7b shows that the stress of B-B is slightly higher than the case of B-A after 0.4% plastic strain. These results show no direct relationship between resolved shear stress and the GB misorientation for present simulated cases. The curves of total dislocation density versus plastic strain for three samples are also plotted in Fig. 7b. As shown in the figure, the total dislocation density of B-C is highest among the three samples. This may explain why

the B-C has the lowest flow stress: since the dislocation density is relatively high in the case of B-C, there might be more mobile dislocations in this bicrystals. In B-C, the forest hardening resulting from dislocation interactions may be weaker than the softening induced by the motion of mobile dislocations, thus rendering a very low resolved shear stress. However, this explanation does not suit for the cases of B-A and B-B, since the dislocation density of B-A is higher than of B-B; meanwhile, the resolved shear stress of B-A is also larger than that of B-B after the plastic strain of ~0.7% (see Fig. 7b). In this case, the forest hardening of dense dislocations may play a dominant role, causing a trend of a higher dislocation density with higher stress.

Fig. 7c presents the total length of absorbed dislocations and the density of emitted dislocation versus plastic strain for three types of pillars. It shows that the overall trend of emitted dislocation density is analogous to that of total dislocation density shown in Fig. 7b, indicating that the density of emitted dislocation plays a significant role in the stress–strain response of these bicrystals. Although the GB strengths are different for these bi-crystalline pillars, they have almost the same absorbed dislocations length at GBs, as shown in Fig. 7c. Fig. 7d plots the distributions of total dislocation density along the Z-direction that is perpendicular to the grain boundary. It can be observed that the dislocation density decreases from the GB to the free surface. The dislocations residing near the GB mainly consist of mobile emitted dislocations and immobile pilling up dislocations from grain interior and emitted dislocations. These dislocations contribute to the softening or hardening of flow stress, depending on the complicated competition between the classical Taylor hardening induced by dislocation interactions and the softening from the motion of mobile dislocations.

From the above analysis, it can be seen that the mechanical responses of the bi-crystalline pillar containing a large-angle symmetric tilt GB investigated here do not depend on (at least do not explicitly depend on) the misorientation angle or the GB strength (or GB energy). Instead, the overall responses of compressive bicrystals are correlated with the complicated GB structure, dislocation–dislocation interactions, dislocation–GB interactions and mobility of dislocations in the samples.
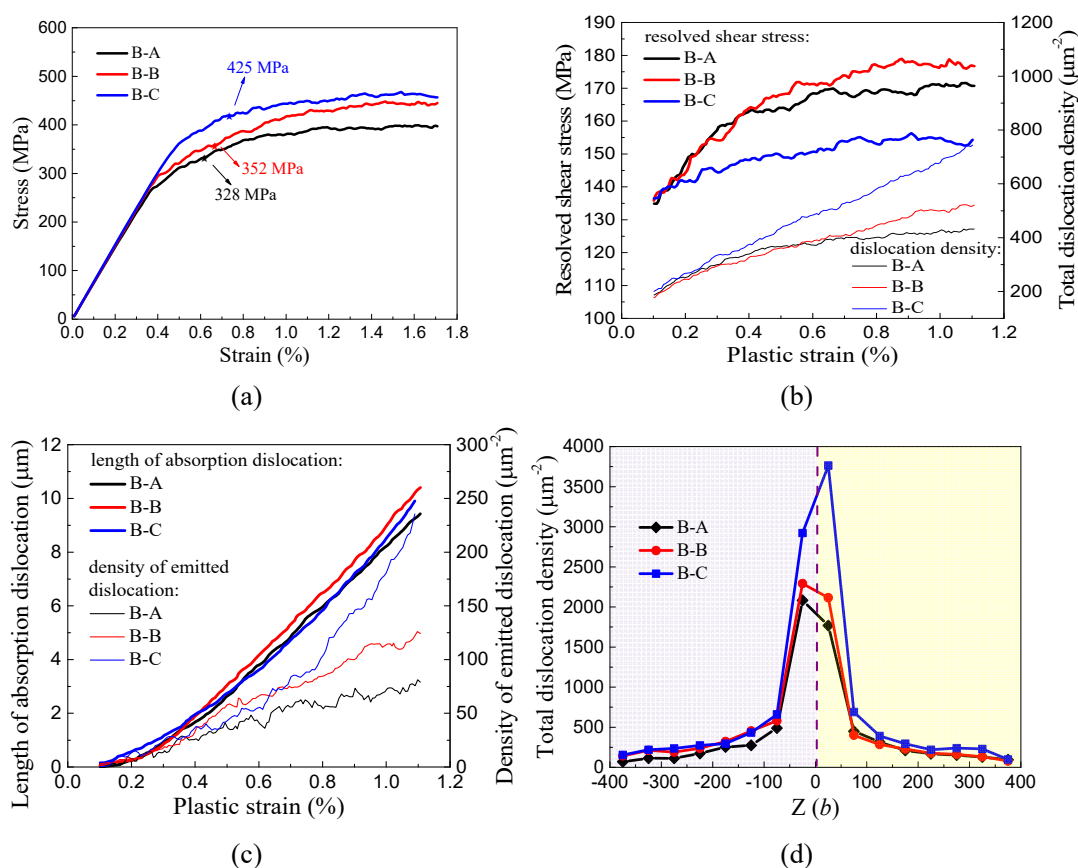
24

Fig. 7. Simulated results of bicrystals A (B-A), bicrystals B (B-B) and bicrystals C (B-C). (a) Stress−strain curves. The solid star symbols marked in the figure are the yield points taken from 0.2% plastic strain. (b) Variations of resolved shear stress and total dislocation density as a function of plastic strain. (c) The total length of absorbed dislocations and density of emitted dislocation versus plastic strain. (d) Distribution of total dislocation density along the Z-axis (normal of GB) at a plastic strain of 1.0%.

5. Conclusions

In current work, a generalized dislocation–GB interaction model applicable for various GB types is developed and introduced into the framework of 3D DDD. In this dislocation–GB interaction model, a 'coarse-graining' method is used to handle the complex dislocation absorption at GBs and dislocation emission from GBs without much loss of physical meanings. In addition, to validate the established dislocation–GB interaction model, the compressive behaviors of bi-crystalline pillars containing a rigid GB and a penetrable GB, together with two single-crystalline counterparts, were simulated and compared with each other. Furthermore, three bi-crystalline nanopillars

25

containing large-angle symmetric tilt GBs with different tilt angles under uniaxial compression were simulated to investigate the effect of GB misorientation on the mechanical behavior of bicrystals. The main findings are summarized as follows:

(1) The strain hardening rate and the flow stress of nanopillars containing a rigid GB are significantly higher than that in the case of penetrable GB, due to the high back stress resulting from severe dislocation pile-ups in front of GB. With the considerations of dislocation absorption at GBs and dislocation emission from GBs in the dislocation–GB interaction model, pillars with a penetrable GB can release stress concentration at the GB and thus lower the flow stress and weaken the strain hardening rate.

(2) The yield stress of the bi-crystalline pillar with a penetrable GB is higher than its constituent single-crystals. The simulation result indicates that, inconsistent with some literature, the higher yield strength of bicrystals does not come from the reduced dislocation length induced by GB obstruction alone. Instead, both dislocation pile-up at GBs and reduced dislocation length contribute to the higher yield stress of the bi-crystalline pillars.

(3) Due to the lack of dislocation emission events, the stress drop size of the bicrystals with a rigid GB is smaller than that of penetrable GB. In addition, the stress drop size in the case of bicrystals with penetrable GB is smaller than that of single crystal, since the dislocation can sweep in a larger area at each dislocation operation in a single crystal. Besides, the stress drop size of a single crystal is related to the crystallographic orientations. More activating slip systems and higher dislocation density during deformation will increase the possibility of dislocation–dislocation interactions and thus leading to smaller drop size.

(4) Neither GB misorientation nor GB strength (or GB energy) has a direct influence on the mechanical responses (such as resolved shear stress, dislocation absorption and emission) of the bicrystals containing a large-angle symmetric tilt GB. The overall flow stress of the bicrystals is a result of the complicated GB structure and the competition between the hardening from forest dislocation interactions and softening from the motion of mobile dislocations in the grain interior.

Finally, it should be mentioned that the dislocation-GB interaction model developed in this work is convenient to be implemented into the polycrystalline discrete dislocation dynamics simulation with a random distribution of grain orientation and arbitrary grain geometry. It is meaningful and valuable to study the mechanical responses and properties of polycrystalline materials using 3D dislocation dynamics, which is the goal of our future work.

References

[1] J. Kacher, B.P. Eftink, B. Cui, I.M. Robertson, Dislocation interactions with grain boundaries, Current Opinion in Solid State and Materials Science 18(4) (2014) 227-243.

[2] D.E. Spearot, M.D. Sangid, Insights on slip transmission at grain boundaries from atomistic simulations, Current Opinion in Solid State and Materials Science 18(4) (2014) 188-195.

[3] L. Zhang, C. Lu, K. Tieu, A review on atomistic simulation of grain boundary behaviors in face-centered cubic metals, Comp Mater Sci 118 (2016) 180-191.

[4] A. Alipour, S. Reese, S. Wulfinghoff, A grain boundary model for gradient-extended geometrically nonlinear crystal plasticity: Theory and numerics, Int J Plasticity 118 (2019) 17-35.

[5] E. Bayerschen, M. Stricker, S. Wulfinghoff, D. Weygand, T. Böhlke, Equivalent plastic strain gradient plasticity with grain boundary hardening and comparison to discrete dislocation dynamics, Proceedings of the Royal Society A: Mathematical, Physical and Engineering Sciences 471(2184) (2015) 20150388.

[6] L. Nicola, Y. Xiang, J.J. Vlassak, E. Van der Giessen, A. Needleman, Plastic deformation of freestanding thin films: Experiments and modeling, J. Mech. Phys. Solids 54(10) (2006) 2089-2110.

[7] L. Nicola, E. Van der Giessen, A. Needleman, Size effects in polycrystalline thin films analyzed by discrete dislocation plasticity, Thin Solid Films 479(1) (2005) 329-338.

[8] R. Schouwenaars, M. Seefeldt, P.V. Houtte, The stress field of an array of parallel dislocation pile-ups: Implications for grain boundary hardening and excess dislocation distributions, Acta Mater 58(13) (2010) 4344-4353.

[9] C. de Sansal, B. Devincre, L.P. Kubin, Grain Size Strengthening in Microcrystalline Copper: A Three-Dimensional Dislocation Dynamics Simulation, Key Engineering Materials 423 (2010) 25-32.

[10] D.S. Balint, V.S. Deshpande, A. Needleman, E. Van der Giessen, Discrete dislocation plasticity analysis of the grain size dependence of the flow strength of polycrystals, Int. J. Plast. 24(12) (2008) 2149-2172.

[11] Z. Li, C. Hou, M. Huang, C. Ouyang, Strengthening mechanism in micro-polycrystals with penetrable grain boundaries by discrete dislocation dynamics simulation and Hall–Petch effect, Comp Mater Sci 46(4) (2009) 1124-1134.

[12] M. Huang, S. Huang, S. Liang, Y. Zhu, Z. Li, An efficient 2D discrete dislocation Dynamics-XFEM coupling framework and its application to polycrystal plasticity, Int J Plasticity 127 (2020) 102647.

[13] S.S. Quek, Z.H. Chooi, Z. Wu, Y.W. Zhang, D.J. Srolovitz, The inverse hall–petch relation in nanocrystalline metals: A discrete dislocation dynamics analysis, J Mech Phys Solids 88 (2016) 252-266.

[14] S.S. Quek, Z. Wu, Y.W. Zhang, D.J. Srolovitz, Polycrystal deformation in a discrete dislocation dynamics framework, Acta Mater 75 (2014) 92-105.

[15] R. Kumar, F. Székely, E. Van Der Giessen, Modelling dislocation transmission across tilt grain boundaries in 2D, Comput. Mater. Sci. 49(1) (2010) 46-54.

[16] N. Ahmed, A. Hartmaier, Mechanisms of grain boundary softening and strain-rate sensitivity in deformation of ultrafine-grained metals at high temperatures, Acta Mater 59(11) (2011) 4323-4334.

[17] C. Zhou, R. LeSar, Dislocation dynamics simulations of plasticity in polycrystalline thin films, Int J Plasticity 30-31 (2012) 185-201.

[18] N. Burbery, G. Po, R. Das, N. Ghoniem, W. Ferguson, Dislocation dynamics in polycrystals with atomistic-informed mechanisms of dislocation-grain boundary interactions, Journal of Micromechanics and Molecular Physics 2(01) (2017) 1750003.

[19] M. Jiang, B. Devincre, G. Monnet, Effects of the grain size and shape on the flow stress: A dislocation dynamics study, Int J Plasticity 113 (2019) 111-124.

[20] H. Fan, Z. Li, M. Huang, Toward a further understanding of intermittent plastic responses in the compressed single/bicrystalline micropillars, Scr. Mater. 66(10) (2012) 813-816.

[21] S. Lu, B. Zhang, X. Li, J. Zhao, M. Zaiser, H. Fan, X. Zhang, Grain boundary effect on nanoindentation: A multiscale discrete dislocation dynamics model, J Mech Phys Solids 126 (2019) 117-135.

[22] Y. Gao, Z. Zhuang, X. You, A hierarchical dislocation-grain boundary interaction model based on 3D discrete dislocation dynamics and molecular dynamics, Science China Physics, Mechanics and Astronomy 54(4) (2011) 625-632.

[23] D. Wei, M. Zaiser, Z. Feng, G. Kang, H. Fan, X. Zhang, Effects of twin boundary orientation on plasticity of bicrystalline copper micropillars: A discrete dislocation dynamics simulation study, Acta Mater 176 (2019) 289-296.

[24] H. Fan, S. Aubry, A. Arsenlis, J.A. El-Awady, The role of twinning deformation on the hardening response of polycrystalline magnesium from discrete dislocation dynamics simulations, Acta Mater 92 (2015) 126-139.

[25] H. Fan, S. Aubry, A. Arsenlis, J.A. El-Awady, Grain size effects on dislocation and twinning mediated plasticity in magnesium, Scripta Mater 112 (2016) 50-53.

[26] B. Liu, D. Raabe, P. Eisenlohr, F. Roters, A. Arsenlis, G. Hommes, Dislocation interactions and low-angle grain boundary strengthening, Acta Mater. 59(19) (2011) 7125-7134.

[27] B. Liu, P. Eisenlohr, F. Roters, D. Raabe, Simulation of dislocation penetration through a general low-angle grain boundary, Acta Mater. 60(13-14) (2012) 5380-5390.

[28] H.M. Zbib, M. Rhee, J.P. Hirth, On plastic deformation and the dynamics of 3D dislocations, International Journal of Mechanical Sciences 40(2) (1998) 113-127.

[29] H.M. Zbib, T. Diaz de la Rubia, A multiscale model of plasticity, Int. J. Plast. 18(9) (2002) 1133-1163.

[30] M. Huang, S. Liang, Z. Li, An extended 3D discrete-continuous model and its application on single- and bi-crystal micropillars, Modelling & Simulation in Materials Science & Engineering 25 (2017).

[31] M. Huang, Z. Li, Coupled DDD–FEM modeling on the mechanical behavior of microlayered metallic multilayer film at elevated temperature, J. Mech. Phys. Solids 85 (2015) 74-97.

[32] H. J.P., L. J., Theory of dislocations, 1982.

[33] X. Zhang, K.E. Aifantis, J. Senger, D. Weygand, M. Zaiser, Internal length scale and grain boundary yield strength in gradient models of polycrystal plasticity: How do they relate to the dislocation microstructure?, J Mater Res 29(18) (2014) 2116-2128.

[34] P.J. Imrich, C. Kirchlechner, C. Motz, G. Dehm, Differences in deformation behavior of bicrystalline Cu micropillars containing a twin boundary or a large-angle grain boundary, Acta Mater 73 (2014) 240-250.

[35] Y. Kim, S. Lee, J.B. Jeon, Y.-J. Kim, B.-J. Lee, S.H. Oh, S.M. Han, Effect of a high angle grain boundary on deformation behavior of Al nanopillars, Scripta Mater 107 (2015) 5-9.

[36] L.L. Li, X.H. An, P.J. Imrich, P. Zhang, Z.J. Zhang, G. Dehm, Z.F. Zhang, Microcompression and cyclic deformation behaviors of coaxial copper bicrystals with a single twin boundary, Scripta Mater. 69(2) (2013) 199-202.

[37] N.V. Malyar, J.S. Micha, G. Dehm, C. Kirchlechner, Dislocation-twin boundary interaction in small scale Cu bi-crystals loaded in different crystallographic directions, Acta Mater. 129 (2017) 91-97.

[38] V. Samaee, S. Sandfeld, H. Idrissi, J. Groten, T. Pardoen, R. Schwaiger, D. Schryvers, Dislocation structures and the role of grain boundaries in cyclically deformed Ni micropillars, Mat Sci Eng A 769 (2020) 138295.

[39] S. Li, L. Yang, C. Lai, Atomistic simulations of energies for arbitrary grain boundaries. Part I: Model and validation, Comp Mater Sci 161 (2019) 330-338.

[40] A. Kunz, S. Pathak, J.R. Greer, Size effects in Al nanopillars: Single crystalline vs. bicrystalline, Acta Mater 59(11) (2011) 4416-4424.

[41] K.S. Ng, A.H.W. Ngan, Deformation of micron-sized aluminium bi-crystal pillars, Philos. Mag. 89(33) (2009) 3013-3026.

[42] N. Kheradmand, A.F. Knorr, M. Marx, Y. Deng, Microscopic incompatibility controlling plastic deformation of bicrystals, Acta Mater 106 (2016) 219-228.

[43] C. Kirchlechner, F. Toth, F.G. Rammerstorfer, F.D. Fischer, G. Dehm, Pre- and post-buckling behavior of bi-crystalline micropillars: Origin and consequences, Acta Mater. 124 (2017) 195-203.

[44] N. Kheradmand, A. Barnoush, H. Vehoff, Investigation of the role of grain boundary on the mechanical properties of metals, Journal of Physics: Conference Series, IOP Publishing, 2010, p. 012017.

[45] X. Zhang, K.E. Aifantis, Accounting for grain boundary thickness in the sub-micron and nano scales, Rev. Adv. Mater. Sci. 26(1-2) (2010) 74-90.

[46] J.R. Greer, J.T.M. De Hosson, Plasticity in small-sized metallic systems: Intrinsic versus extrinsic size effect, Prog. Mater. Sci. 56(6) (2011) 654-724.

[47] F. Roters, M. Diehl, P. Shanthraj, P. Eisenlohr, C. Reuber, S.L. Wong, T. Maiti, A. Ebrahimi, T. Hochrainer, H.O. Fabritius, S. Nikolov, M. Friák, N. Fujita, N. Grilli, K.G.F. Janssens, N. Jia, P.J.J. Kok, D. Ma, F. Meier, E. Werner, M. Stricker, D. Weygand, D. Raabe, DAMASK – The Düsseldorf Advanced Material Simulation Kit for modeling multi-physics crystal plasticity, thermal, and damage phenomena from the single crystal up to the component scale, Comp. Mater. Sci. 158 (2019) 420-478.

[48] X. Lu, X. Zhang, M. Shi, F. Roters, G. Kang, D. Raabe, Dislocation mechanism based size-dependent crystal plasticity modeling and simulation of gradient nano-grained copper, Int. J. Plast. 113 (2019) 52-73.

[49] M.A. Tschopp, D.L. McDowell, Asymmetric tilt grain boundary structure and energy in copper and aluminium, Philos. Mag. 87(25) (2007) 3871-3892.

[50] D.E. Spearot, M.A. Tschopp, K.I. Jacob, D.L. McDowell, Tensile strength of ⟨100⟩ and ⟨110⟩ tilt bicrystal copper interfaces, Acta Mater 55(2) (2007) 705-714.

[51] C.L. L Zhang, K Tieu, X Zhao, L Pei, The shear response of copper bicrystals with Σ11 symmetric and asymmetric tilt grain boundaries by molecular dynamics simulation, Nanoscale 7(16) 7224-7233.

[52] X. Tong, H. Zhang, D. Li, Effects of misorientation and inclination on mechanical response of< 1 1 0> tilt grain boundaries in α-Fe to external stresses, Model Simul Mater Sc 22(6) (2014) 065016.

[53] L. Zhang, C. Lu, K. Tieu, Molecular Dynamics Simulation on Σ5 Grain Boundaries of Copper Bicrystal under Tensile and Shear Deformation, MRS Proceedings 1651 (2014) mrsf13-1651-kk12-06.

[54] L. Zhang, C. Lu, K. Tieu, L. Pei, X. Zhao, K. Cheng, Molecular dynamics study on the grain boundary dislocation source in nanocrystalline copper under tensile loading, Materials Research Express 2(3) (2015) 035009.